GEOPHYSICS, VOL. 72, NO. 4 (JULY-AUGUST 2007); P. B93–B106, 21 FIGS.
10.1190/1.2729473

Case History

Local high-resolution passive seismic tomography and Kohonen neural networks — Application at the Rio-Antirrio Strait, central Greece

G-Akis Tselentis[1], Anna Serpetsidaki[1], Nikolaos Martakis[2], Efthimios Sokos[1],
Paraskevas Paraskevopoulos[1], and Sotirios Kapotas[3]

ABSTRACT

A high-resolution passive seismic investigation was performed in a 150 km^2 area around the Rio-Antirrio Strait in central Greece using natural microearthquakes recorded during three months by a dense, temporary seismic network consisting of 70 three-component surface stations. This work was part of the investigation for a planned underwater rail tunnel, and it gives us the opportunity to investigate the potential of this methodology. First, 150 well-located earthquake events were selected to compute a minimum (1D) velocity model for the region. Next, the 1D model served as the initial model for nonlinear inversion for a 3D P- and S- velocity crustal structure by iteratively solving the coupled hypocenter-velocity problem using a least-squares method. The retrieved V_p and V_p/V_s images were used as an input to Kohonen self-organizing maps (SOMs) to identify, systematically and objectively, the prominent lithologies in the region. SOMs are unsupervised artificial neural networks that map the input space into clusters in a topological form whose organization is related to trends in the input data. This analysis revealed the existence of five major clusters, one of which may be related to the existence of an evaporite body not shown in the conventional seismic tomography velocity volumes. The survey results provide, for the first time, a 3D model of the subsurface in and around the Rio-Antirrio Strait. It is the first time that passive seismic tomography is used together with SOM methodologies at this scale, thus revealing the method's potential.

INTRODUCTION

In past years, 3D models of V_p and V_p/V_s derived from surface passive seismic methodologies have proved useful to investigate the structure of fault systems and have contributed to our understanding of seismotectonics and seismogenic processes over large areas mainly for crustal studies (Thurber et al., 1995; Eberhart-Phillips and Michael, 1998; Chiaraba and Amato, 2003).

Recent advances in seismograph design, monitoring methodologies, and inversion algorithms have resulted in the application of passive seismic methods to the hydrocarbon industry as well. Passive seismic methods have for sometime been applied to reservoir characterization projects and fault and fracture location and orientation. Using tomography at this local scale requires a different field setup and operational considerations that follow more or less the logic of 3D seismic surveys. Passive seismic tomography has been successfully applied for hydrocarbon exploration, thus showing its potential to map large regions for a relatively low cost compared to conventional 3D seismic surveys (Kapotas et al., 2003; Durham, 2003; Martakis et al., 2006).

The Rio-Antirrio Strait exhibits high observed rates of continental crustal deformation accompanied by very high seismic activity (Figure 1). Numerous seismological, geodetic, and neotectonic studies have been reported in the area (e.g., Tselentis and Makropoulos, 1986; Brooks et al., 1988; Melis et al., 1995; Rigo et al., 1996; Le Meur et al., 1997; Latorre et al., 2004; Lyon-Caen et al., 2004).

Although many tectonic models have been proposed for the Rio-Antirrio Strait, the relationship between lithological variations at depth and the major faults is not well understood (e.g., Doutsos and Poulimenos, 1992; Sorel, 2000).

Manuscript received by the Editor September 13, 2006; revised manuscript received January 11, 2007; published online May 9, 2007.
[1] University of Patras, Seismological Laboratory, Rio, Greece. E-mail: tselenti@upatras.gr, annaserp@geology.upatras.gr, esokos@upatras.gr, paris@geology.upatras.gr.
[2] LandTech Enterprises, Athens, Greece. E-mail: nmartakis@landtechsa.com.
[3] LandTech Enterprises, Cardiff Bay, United Kingdom. E-mail: skapotas@landtechsa.com.
© 2007 Society of Exploration Geophysicists. All rights reserved.

The high seismicity of the region makes it a favorable target to exploit the potential of passive seismic tomography methodologies. The goal of this field experiment was to collect a high-quality, local earthquake data set and to produce models of the 3D crustal structure, thereby adding more constraints to define and consistently interpret the crust in this region. The main objectives of this investigation (which was part of a feasibility study for a planned tunnel below the Rio-Antirrio Strait) were the accurate estimation of the thickness of Quaternary and Neogene formations, the mapping of the basement, and the identification of active faults. This survey also provided a good opportunity to explore the potential of passive seismic methodologies and their possible application in hydrocarbon exploration projects as well.

Passive seismic tomography is characterized by three main advantages over conventional seismic methodologies: it is cost effective, it is environmentally friendly, and it is easily applicable even in areas with the most difficult terrain.

Because this was the first time that such a high-resolution, passive seismic investigation was undertaken at such a local scale, special care was devoted to testing the robustness of our 3D inversion.

GEOLOGIC AND TECTONIC SETTING

The study area covers the Rio-Antirrio Strait (Figure 2), which is located in the northern part of the Peloponnesus. The Corinth and Patras rifts are linked by transfer faults in the Rio-Antirrio Strait (Doutsos and Poulimenos, 1992). After Middle Miocene, the whole northwest Peloponnesus area was uplifted and extended. During this extension, three asymmetric grabens were formed: the Corinth, Rio-Antirrio, and Patras grabens. The asymmetry of the grabens is largely induced by north-dipping master faults, which trend parallel to the coastline of the North Peloponnesus (Doutsos and Poulimenos, 1992). In the Quaternary, rifting propagated westward until it reached the Rio-Antirrio graben. The Rio graben, formed by movement on pre-existing northeast-southwest trending faults, reactivated in the Pliocene (Doutsos et al., 1985). Changes in predominant stress directions at this time led to the Rio graben acting as a transfer zone between the extending Patras and Corinth grabens (Tselentis and Makropoulos, 1986; Doutsos et al., 1988).

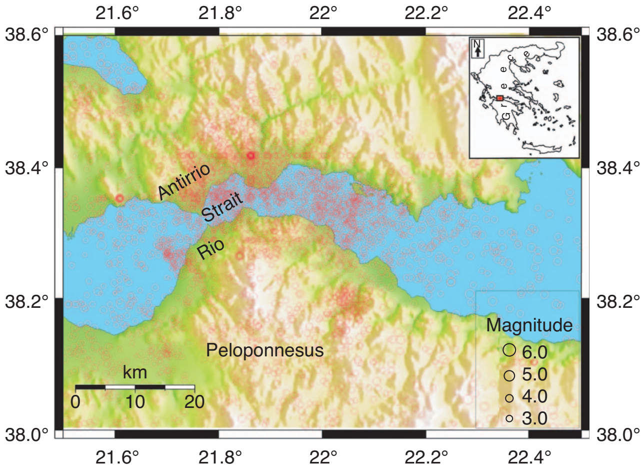

Figure 1. Earthquake activity from 1995 to 2005 in the Rio-Antirrio region as it was recorded by Patras University Seismological Center.

EARTHQUAKE DATA AND PROCESSING

The selected area for the tomographic inversion is localized around the Rio-Antirrion Strait and spans over a 10 × 15-km area (Figure 3). A microearthquake network, consisting of 70 EarthData PR24 recording stations supplemented with LandTech LT-S01 three-component velocity sensors, was deployed during a three-month seismic experiment in the autumn of 2004. We attempted to deploy the network over a grid with an average spacing between nodes of 500 m (Figure 3). Station coordinates were established by differential GPS measurements with a horizontal accuracy of ± 2 m and a vertical accuracy of ± 1 m. Time sampling was 200 samples per second.

The various stages of data processing for surface passive seismic tomography that are used in the present investigation are summarized in Figure 4.

Our initial data set consisted of 9330 P-wave and 5591 S-wave arrival-time readings, which corresponded to 220 local microearthquake events with magnitudes M_L ranging between – 0.5 R and 3.0 R, except for one earthquake located in the Antirrio fault area with magnitude 4.5 R. P- and S-wave arrival times were observed from digital seismograms using the interactive seismogram processing algorithm developed by Xanalatos and Tselentis (1997). Time picking accuracy was estimated to be between 0.05 and 0.06 s for P and 0.01

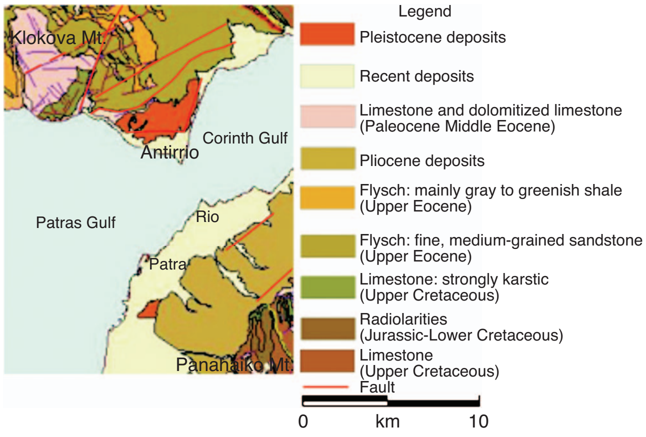

Figure 2. Generalized geology of the Rio-Antirrio Strait region.

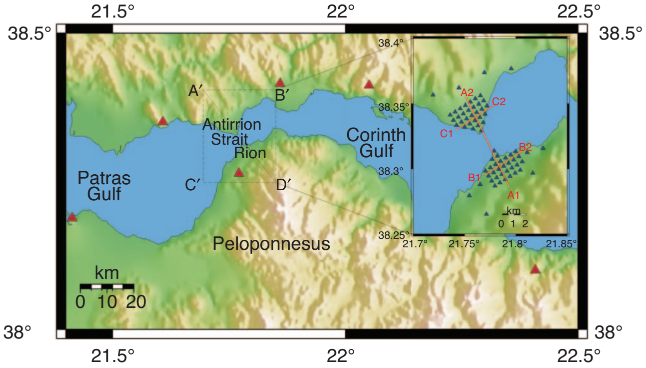

Figure 3. Microseismic network design. Small triangles in inset depict the location of the seismographs. Red triangles show the out-of-the-region installed stations used to locate peripheral events and increase ray coverage within the region of interest.

and 0.1 s for S first-arrival times. A preliminary hypocenter location was performed following Lahr's (1989) methodology, and a multiple layer, 1D velocity model was derived from the literature (Hatzfeld et al., 1996; Rigo et al., 1996; Tselentis et al., 1998; Haslinger et al., 1999; Tselentis and Zahradnik, 2000; Novotny et al., 2001; Latorre et al., 2004).

Derivation of 3D inversion model

Because any linearized 3D inversion may be affected strongly by the initial reference velocity model, we have used the procedure suggested by Kissling et al. (1994) and Kradolfer (1989) to find a reference 1D velocity model that relies on our seismic and other published data. We first establish a smooth, a priori 1D model that approximately explains the observations and accounts for the geological evidence and for other published data for the region. This initial 1D model is then further refined until the predictions of traveltime match the observations to a sufficient degree.

Traveltime data are jointly inverted with the hypocenter coordinates and station corrections starting from an a priori reference model. An inappropriate choice of the 1D reference model may give rise to artifacts in the inversion results. Thus, we used, as a priori information, the P- and S-velocity models (Figure 5a and b) suggested by previous researchers in the region (Hatzfeld et al., 1996; Rigo et al., 1996; Bernard, 1997; Le Meur et al., 1997; Melis and Tselentis, 1998; Latorre et al., 2004, Lyon-Caen et al., 2004).

Next, we digitized, at every 2 km, the published 1D P- and S-velocity models and estimated an average initial model to start the 1D inversion (Figure 5a and b). The construction of the initial 1D model for the area was done after selecting data for quality because uncertainties in hypocenter locations will introduce instabilities in the inversion process. We considered only events for which at least nine observations (traveltime readings) were available, and for which the rms traveltime residuals were less than 0.3 s.

Also, to improve data quality, we have eliminated all S-wave arrival readings that are on only one-component records and are present at less than five stations. This procedure improves the global quality of our data set (Latorre et al., 2004). Following the application of these criteria, we retained 150 events corresponding to 8840 P-wave and 5381 S-wave arrivals that occurred within or near the target area.

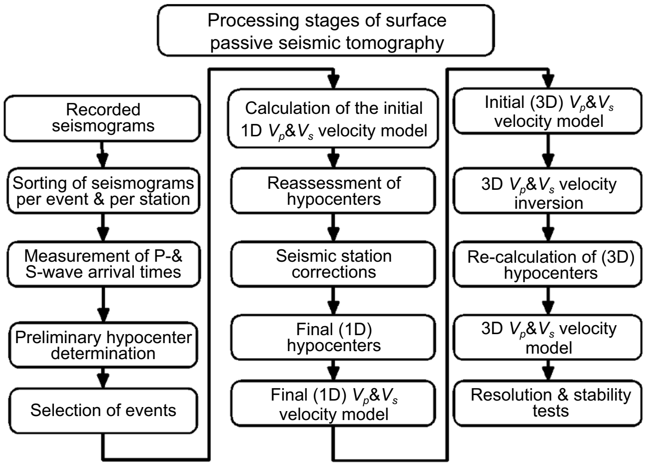

Figure 4. Flow chart presenting the data processing used in the present investigation.

During this inversion process, we combined layers for which velocities converge to similar values and obtained the final layering of the initial 1D P- and S-velocity model (Figure 6a and b). The average rms residual for the located events after the initial 1D velocity model inversion was 0.087s.

To ensure robustness of the tomographic results with respect to our choice of the initial velocity model, we performed several numerical tests. The 1D initial model selected is accurate enough to lead to a reliable 3D final model (Tselentis and Stavrakakis, 1987; Kissling et al., 1995; Latorre et al., 2004).

The procedure described by Latorre et al., 2004, was followed throughout this investigation. The inversion started by defining two (extreme) initial models with average velocities significantly higher or lower than the initial 1D P-model (Figure 6a) and the 1D S-model (Figure 6b). Then, we randomly extracted 100 1D P- and S-velocity models by always requiring a positive, local vertical gradient. All these 1D models give initial rms residual values ranging between

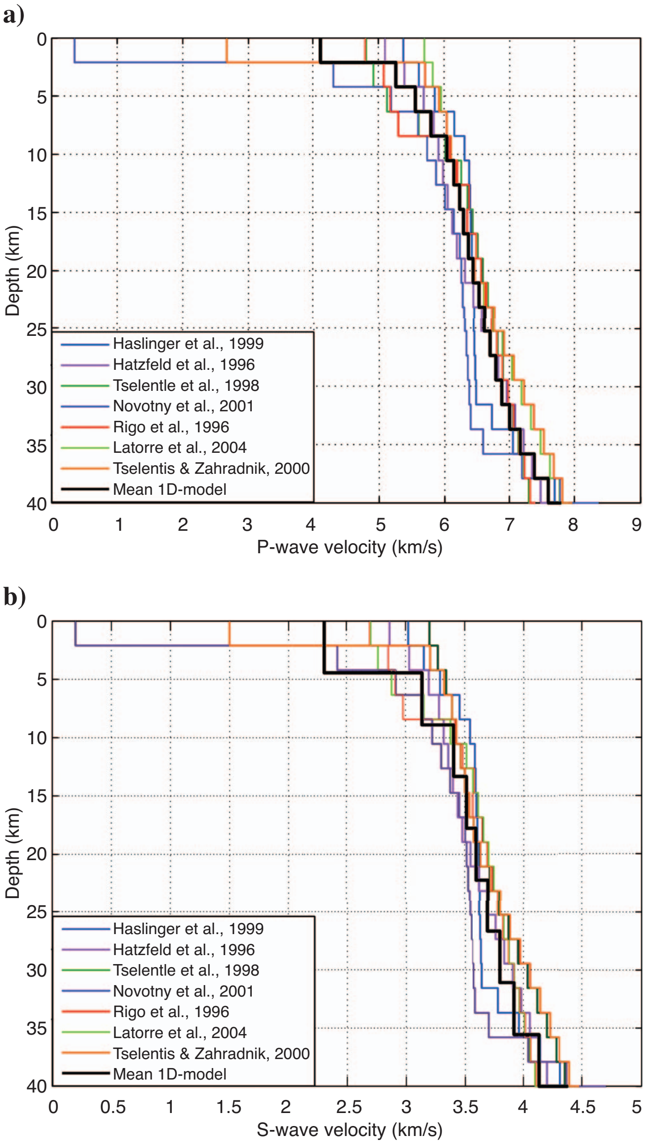

Figure 5. Published 1D (a) V_p and (b) V_s models for the region. Calculated average models are depicted by bold lines.

0.022 and 0.91 s, which shows a sufficient sampling of the 1D input model space. Then we performed a 3D tomographic inversion by starting from the initial random models. On the basis of the final 3D velocity models, the average rms residual for the relocated seismic events, was reduced to 0.057 s. The rms distribution for the range 0 to 0.25 s, before and after the 3D inversion, is presented in Figure 7. Next, we selected the 10 best 3D models (10% of the random models) and estimated the differences with respect to their average velocity model. This represents the variability of the inversion results with respect to the initial model selection.

These 10 best inversion models show a variability of less than 10%. This estimated variability of the selected 3D best models is very low if we consider the large range of the randomly selected initial velocity models. Because our selected 1D model falls into the initial sampling model space, and provides both the lowest initial data misfit and lowest final data misfit for the 3D inversion, we strongly believe that our tomographic results are minimally dependent on the initial model selected.

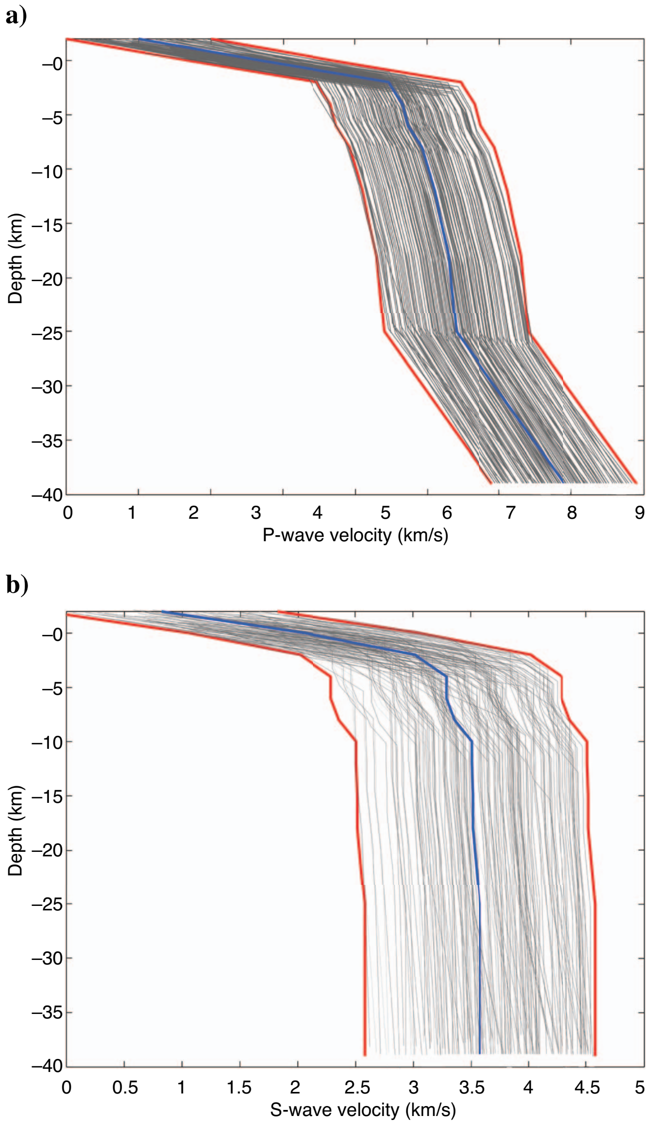

Figure 6. Initial 1D (a) V_p and (b) V_s models obtained from the inversion (blue lines). Red lines depict minimum velocity models ± 1 km/s.

Local earthquake tomography

Local earthquake tomography has become a well-established technique since its introduction in the mid 1970s. Comprehensive reviews of different aspects of the method are found in Thurber (1986), Kissling (1988), and Iyer and Hirahara (1993). Because seismic instrumentation in older networks is mostly vertical component, most 3D tomography inversions have involved only P-waves and have simultaneously inverted for the velocity structure and the hypocenter location (e.g., Toomey and Foulger, 1989). Other researchers (e.g., Benz et al., 1996) initially invert for P-wave velocity structure and hypocentral locations, and, in a subsequent inversion for the S-wave velocity structure, the hypocentral parameters are fixed.

Apart from the general interest of also knowing the S-wave velocity structure, the use of S-arrivals in addition to P-arrivals improves the hypocenter locations, especially the source depths (Gomberg et al., 1990). Where the S-wave data are less numerous than the P-wave data and of poorer quality, an inversion of the P-velocity and V_p/V_s ratio along the P-wave rays may be justified (e.g., Thurber, 1993; Eberhart-Phillips and Reyners, 1997). On the other hand, when the S-wave data are of similar quality and number as the P-wave data, a simultaneous inversion of the P- and S-waves is preferable, and the V_p/V_s ratio variation is controlled by damping the V_p/V_s ratio (Michelini, 1993; Tryggvason et al., 2002).

In the present investigation, the data were inverted using the technique of Thurber (1993) and that of Eberhart-Phillips and Reyners (1997). This technique uses an iterative, damped least-squares method to invert arrival times, simultaneously estimating earthquake locations and 3D V_p and V_p/V_s fields (e.g., Martakis et al., 2006). The wave speeds are parameterized by values defined at the nodes of a 3D grid, between which the V_p and V_p/V_s values are interpolated with trilinear functions.

The 3D ray tracing in this analysis follows the method of Eberhart-Phillips (1990) in which an initial raypath is obtained using Thurber's (1983) approximate 3D ray tracing and, then, an iterative

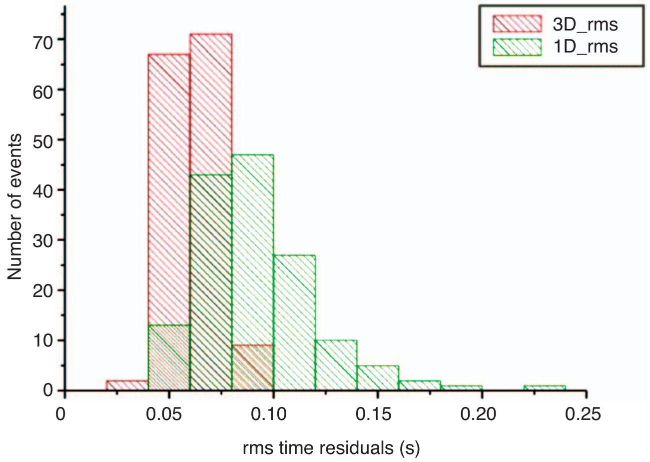

Figure 7. The rms distribution of seismic events for initial 1D velocity model (green) and 3D velocity model (red).

pseudobending approach (Um and Thurber, 1987) is applied. Hypocenter locations are updated using the new velocity model at each iteration step.

To obtain a well-constrained velocity structure, we have performed several inversions by varying the model parameterization grid as well as the starting velocity model. This procedure allows separation of well-recovered heterogeneities from artifacts or ghost images, which might depend on the starting velocity model, the grid parameterization, and the limited spatial sampling.

Model parameterization of the velocity field should be able to delineate the shape and position of heterogeneities. A nodal representation in which the velocity field is reconstructed by a 3D grid does not assume a specific geometry of heterogeneities (Latorre et al., 2004; Toomey and Foulger, 1989). Nevertheless, node positions control the tomographic inversion solution. Ray coverage, which mainly depends on the station/earthquake distribution, limits the spacing between nodes of the inversion grid to be selected for optimum resolution. Therefore, our choice of the optimal grid mesh has been determined as a function of the acquisition/event geometry.

During the experiment, stations were densely distributed all around the Rio-Antirrio Strait with an average spacing of 500 m (Figure 3). No ocean bottom seismometers were located in the gulf, thus reducing our acquisition coverage between the southern and the northern coast, whose epicentral distance spans from 3 to 8 km. We have tested different grid spacings to find the best compromise between model parameterization, spatial resolution, and a reliable representation of the velocity structure.

These tests demonstrate that a graded 3D inversion scheme may overcome the ray coverage problem in the offshore part of the study area. The first step of this procedure was the construction of a velocity model for the whole network area using a grid of evenly spaced nodes with dimensions of $1 \times 1 \times 1$ km. The resulting 3D model was used as a starting model in the second step where we used a grid of nodes with dimensions $0.5 \times 0.5 \times 0.5$ km for the inversion only in the target area.

Fitting of delay times requires a damping term to obtain physically plausible velocity variations and earthquake distributions. The choice of a damping value for the 3D inversion was based on a series of tests on the trade-off between model variance and data variance (Eberhart-Phillips, 1986). For a large range of damping values, inversions of one iteration were conducted. From these tests, by plotting data variance against model variance, a damping value of 10 has been chosen in which we achieved a considerable reduction of data variance with only a modest increase in model variance. With lower damping values, a rather limited decrease of data variance is paid by rapidly increasing model variance.

Resolution tests

The minimization of the arrival-time residuals is an iterative procedure including the solution of the forward and inverse problem at each step. The linearized inversion can be written in a matrix notation as (e.g., Lee and Stewart, 1981; Thurber, 1983; Martakis et al., 2006)

$$\Delta\mathbf{m}^{\text{est}} = \mathbf{G}^{-1}\Delta\mathbf{d} = \mathbf{R}\Delta\mathbf{m}^{\text{true}}, \tag{1}$$

where $\mathbf{G}$ is the Jacobian matrix that contains all the partial derivatives of traveltimes from earthquake hypocenters to the recording seismograph, $\mathbf{m}^{\text{est}}$ is the estimation for the model, $\mathbf{m}^{\text{true}}$ is the real model, and $\mathbf{R}$ is the model resolution matrix. The perturbation of the model parameters $\Delta\mathbf{m}$ expresses the disturbances of the data $\Delta\mathbf{d}$ (e.g., Lee and Stewart, 1981; Thurber, 1983), i.e.,

$$\Delta\mathbf{d} \approx \mathbf{G}\Delta\mathbf{m}. \tag{2}$$

In practice, the problem of passive tomography is usually underdetermined or mixed determined. For this reason, the method of solution is the damped least-squares method, which is

$$\Delta\mathbf{m} = (\mathbf{G}^T\mathbf{G} + \varepsilon^2\mathbf{I})^{-1}\mathbf{G}^T\Delta\mathbf{d}, \tag{3}$$

where ε^2 is the damping factor and $\mathbf{I}$ is the identity matrix.

Many techniques have been proposed in previous studies to estimate model fidelity or resolution in earthquake tomography. The most common methods are the calculation of the hit count, the derivative weighted sum (DWS), and the resolution diagonal elements (RDE). The hit count is the summation of the number of rays which pass through the region-of-influence of a model parameter. The DWS provides a more reliable estimation of the sampling of the study area because it sums up all the ray segment lengths in the region-of-influence of one velocity parameter, weighting them according to the distance from it, and is defined as (Toomey and Foulger, 1989)

$$\text{DWS}(a_n) = N\sum_i \sum_j \left(\int_{Pij} \omega_n(x)ds \right), \tag{4}$$

where i and j are the event and station indices, ω_n is the weight used in the linear interpolation and depends on coordinate position, P_{ij} is the raypath between i and j, N is a normalization factor that takes into account the volume influenced by a_n, and ds is the segment along the raypath. The quantity DWS quantifies the relative ray density in the volume-of-influence of a model node, weighting the importance of each ray segment by its distance to the model node. It yields a rough estimate of the illumination of the model space.

The RDE are the diagonal elements of the resolution matrix $\mathbf{R}$, which is described by equations 1 and 3. These equations result from the SVD solution of equation 2 (Lanczos, 1961); by replacing $\mathbf{G}$ by its fundamental decomposition, $\mathbf{R}$ becomes

$$\mathbf{R} = \mathbf{V}\left(\frac{\mathbf{\Lambda}^2}{\mathbf{\Lambda}^2 + \varepsilon^2\mathbf{I}} \right)\mathbf{V}^T, \tag{5}$$

where $\mathbf{V}$ is a matrix whose columns are coupled-parameter-space eigenvectors, $\mathbf{\Lambda}$ is the matrix of nonzero eigenvalues, and $\mathbf{I}$ is the identity matrix. Each row of $\mathbf{R}$ describes the dependence of the solution for one model parameter on the other model parameters. As a first-order global diagnostic tool, we can use the sum of the diagonal elements of $\mathbf{R}$ (RDE) that corresponds to

$$\text{RDE} = \mathbf{R}_{\text{diag}} = \frac{\mathbf{\Lambda}^2}{\mathbf{\Lambda}^2 + \varepsilon^2\mathbf{I}}. \tag{6}$$

The full-resolution matrix offers important information about the quality of the inversion results. Each row of matrix $\mathbf{R}$ describes the dependence of one model parameter on all the other parameters of the model. Although the resolution matrix can be used to check the quality of the tomography results, it is computationally very consuming to interpret it. Therefore, instead, the RDE is commonly used to assess solution quality. The larger the RDE is for the model parameters, the more independent are the solutions.

The hit count is a crude measure of the study volume's sampling because it does not use any information about the ray segment length in the vicinity of a model parameter or about the weight of the observation. The DWS depends on the ray segment length, the RDE and the spread on the grid spacing, and the damping value used in the inversion process (Eberhart-Phillips, 1986; Toomey and Fougler, 1989).

An appropriate method to estimate the reliability of the tomography results is based on the evaluation of reconstructed, synthetic checkerboard models for the specific experiment geometry (e.g., Humphreys and Clayton, 1988). The advantage of this procedure is that it can give information about the effects of the model grid spacing and the distribution of the data. In addition, it is able to estimate how close the calculated model parameters are to the initial absolute values.

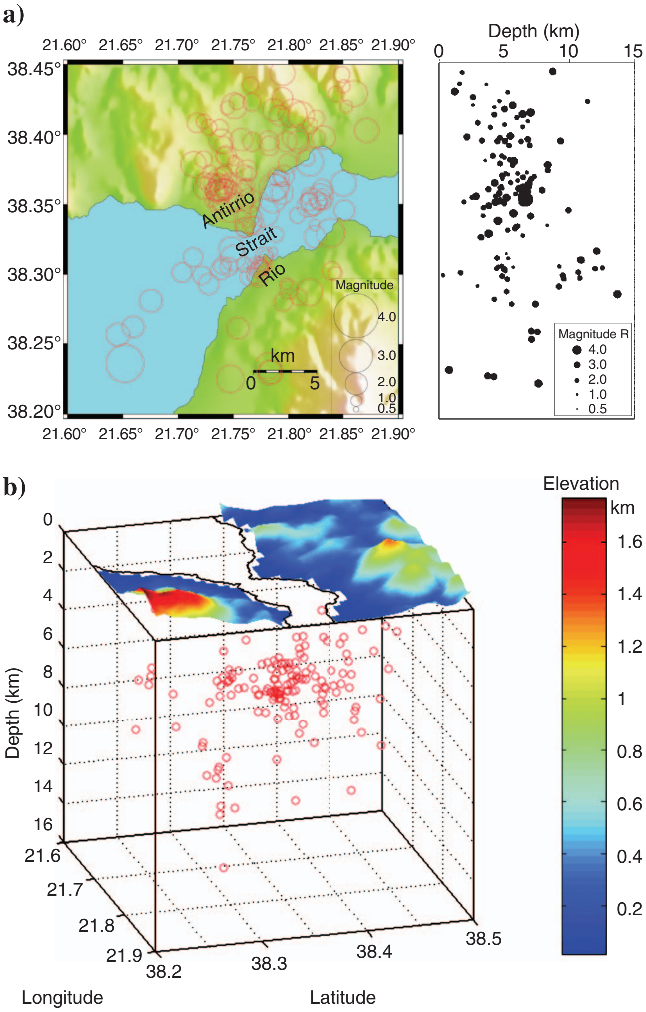

Figure 8. (a) Epicenters of located earthquakes over the entire Rio-Antirio Strait and the hypocenter distribution versus depth projected along a north-south vertical plane; (b) 3D view of the recorded seismicity.

EARTHQUAKE LOCATIONS AND P- AND S-VELOCITY INVERSION

Velocity inversion results and geology

Figure 8 shows 2D and 3D views of the located earthquakes. Hypocentral locations of the earthquakes extend to 15 km depth, but most of the events were located between 2 and 9 km. Although microseismicity is very intense, very low seismicity is observed in the first 2 km of the crust. Furthermore, most of the located events seem to lie outside of the installed dense network (Figure 8a). This event distribution may have influenced our tomographic results; hence, we expect to have both a better spatial resolution and a higher accuracy in the deeper part of retrieved tomographic models compared to that in the shallower part unless we use some shallow peripheral events located at the outskirts of the investigated region in the inversion process. For this reason, for the accurate location of the peripheral events, we used recordings at six additional stations (Figure 3) installed beyond the immediate region of interest.

Earthquake events distribution

Next, we calculated V_p and Poisson's models of the investigated area. Figures 9a and b show a 2D cross section of V_p and Poisson's ratio across the strait from Rio to Antirio. Similar cross sections, but in an almost northeast-southwest direction, are presented in Figures 10a and b and 10c and d for Rio and Antirrio, respectively. Figure 11a

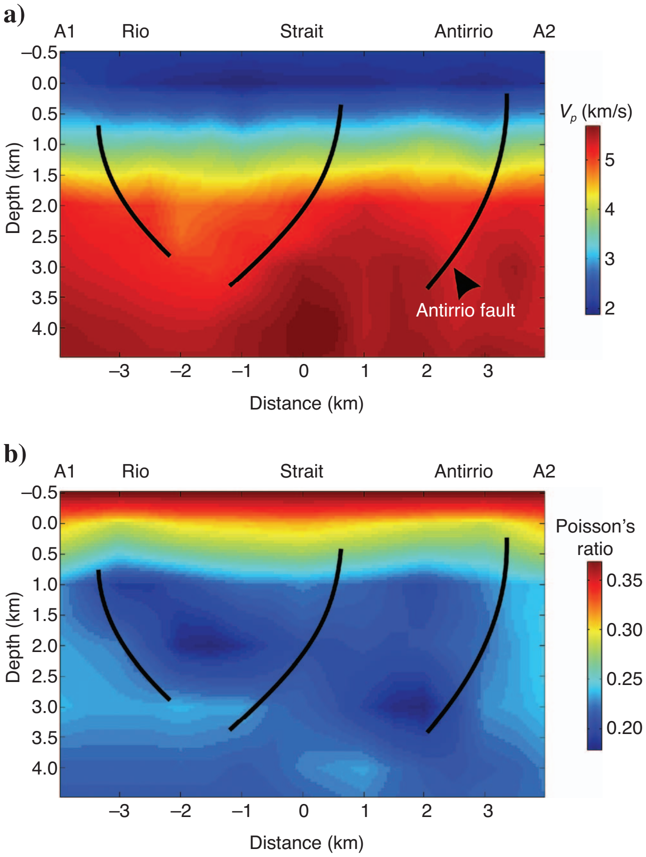

Figure 9. (a) Cross section of V_p velocity model and (b) corresponding Poisson's ratio along profile A1–A2 in Figure 3. The black lines are interpreted faults.

shows a 3D view of the resulting V_p model; V_p values of <3 km/s and a Poisson's ratio of >0.26 ($V_p/V_s > 1.9$) correspond to Quaternary and Neogene formations. The thickness of these formations in the target area is approximately 500–600 m (Figures 9 and 10), which agrees with previous geological studies (Kontopoulos and Doutsos, 1985). Also, shallow drillings, down to 100 m below the sea bottom, for the construction of the Rio-Antirrio Bridge are consistent with these results; they indicate the presence of Quaternary formations (i.e., sand and gravel, clay, silt). Here, P-wave velocities >5.2 km/s and V_p/V_s values of 1.8 correspond to limestone (Martakis et al., 2006) and characterize the alpine basement. To get a 3D view of the basement over the investigated area, we have kept all P-wave velocities >5.2 km/s and have plotted them in Figure 11b. The most obvious features are the Rio graben and the Antirrio fault zone at the northern part of the network.

Figure 12 shows plan views of the V_p and V_p/V_s models at 0 and 3 km depth. The comparison of tomography results at 0 km depth (Figure 12a) to the surface geology (Figure 2) reveals that low-velocity anomalies represent the thick sedimentary formations, whereas high-velocity anomalies represent sites where bedrock outcrops or lies under a thin layer of sediments. In the northwestern part of the study area, high velocities represent the limestone Klokova Mountain (Figure 2). The high velocities in the northern and northeastern part of the study area represent the flysch formations of the Pindos zone. In the southern part of the study area, the high-velocity anomaly represents the foot of Panahaikon Mountain (Figure 2) where limestone and radiolarites crop out. Low velocities at the Rio site represent Pliocene and Recent deposits.

A comparison of the major active faults of the study area (Figure 2) to the slices in Figures 12a and b indicates that active tectonics controls the velocity distribution in the upper crust. The faults in Antirrio form the small depression in the area and disrupt the bedrock volume. The faults at the Rio site define the southern boundary of the basin (Figure 11b).

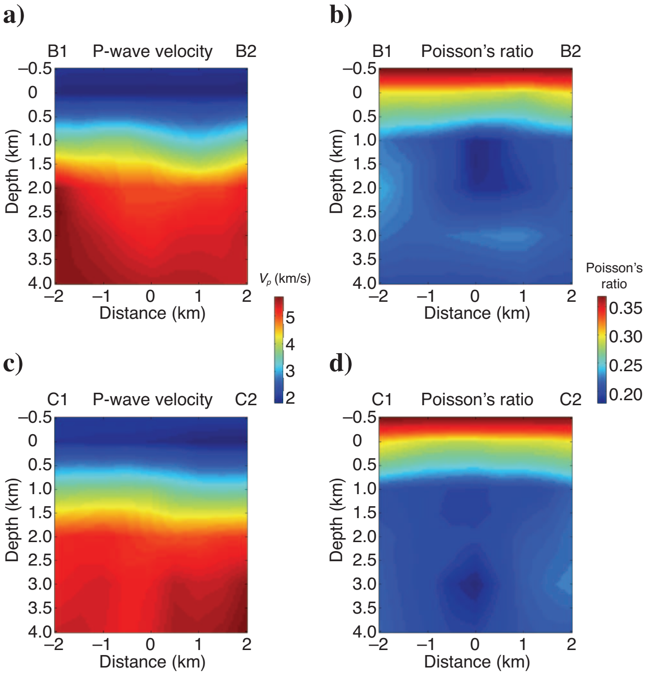

Figure 10. Cross sections of V_p and Poisson's ratio along profiles B1–B2, and C1–C2 in Figure 3.

The cross sections along (Figure 9a) and across (Figure 10b and c) the Rio-Antirrion axis show that, at both Rio and Antirrio, low-velocity anomalies correspond to thick sediments that lie in the depressions formed by the major faults. The low-velocity anomalies are more apparent at Rio and Antirrio than in the strait between the sites where sedimentation is limited.

The velocity distribution in the Antirrio area indicates that the basin was formed by more than two faults. The Rio sediments appear to be thicker than those of Antirrio, and their existence is obvious, even in the plane at 2 km depth. Figure 11b shows that the basin at Rio is deeper than that at Antirrio, in agreement with the morphology of the Rio-Antirrio graben (Flotte et al., 2005).

The southern part of the study area, Rio, is located to the north of the foot of Panahaikon Mountain (Figure 2). The northeast-southwest trending fault system (Figure 11b, region R), which is called the Rio-Patras fault zone, is parallel to the Panahaikon. The Rio-Patras faults present clear characteristics of a recent, and probably active,

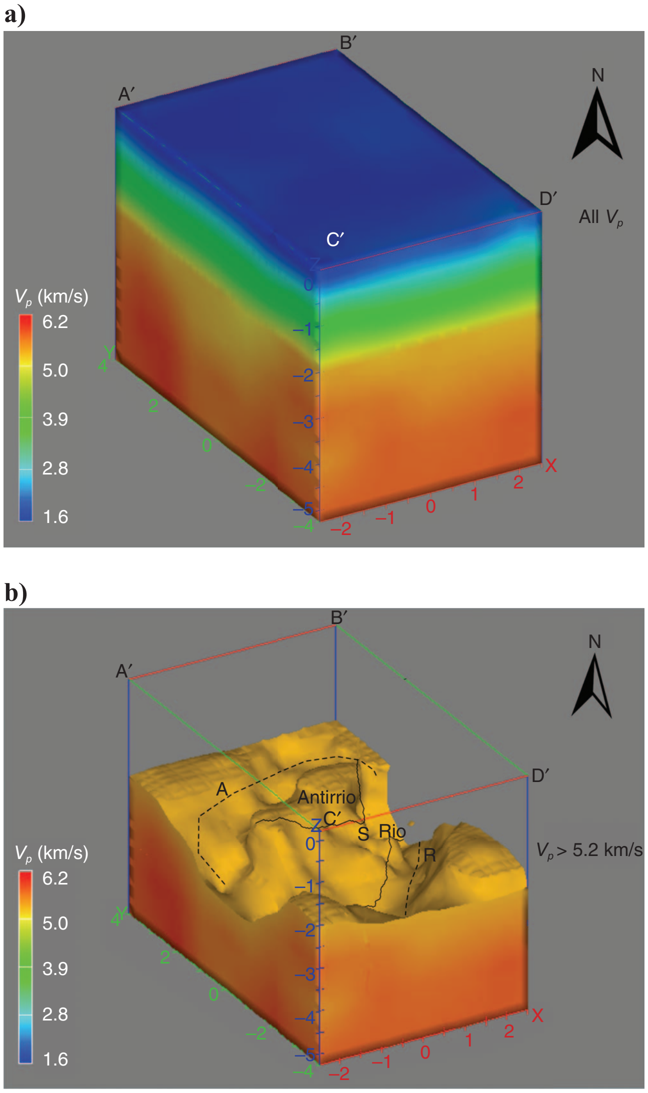

Figure 11. (a) Three-dimensional view of the V_p velocity model of the investigated region. (b) Three-dimensional view of the V_p velocity model after removing all formations with velocities <5.2 km/s and showing structural details of the area.

fault zone. This vertical offset of ca. 1.4 km on the Rio-Patras faults supports an extension rate of 0.8 to 1 cm a year during the last 200 thousand years (Flotte et al., 2005).

The northern part of the study area is the Antirrio site. The post-Alpidic history of the Antirrion area begins with isostatic uplift and synchronous development of a northeast trending fault zone transverse to the Alpidic folded basement. In the resulting depressions, thick marine-lagoonal and lacustrine strata accumulated (Figure 11b, region A). Yellowish strata are interpreted as overbank silts and braided-river gravels, and reddish strata, as debris-flow sediments and water-laid sediments on alluvial fans (Kontopoulos and Doutsos, 1985). Plio-Quaternary sediments of the Antirrion area crop out in low hills to the south of a major east-west fault, which marks the boundary with the Alpidic rocks.

Water depths reach 135 m along the axis of the Patras basin and shoal dramatically northeastwards towards the Rio-Antirrio Strait. The bathymetry is controlled by extensive active faulting of west-northwest-east-southeast trend (Ferentinos et al., 1985). The Rio Strait has no upper Pleistocene sediment and exposes complexly faulted lower Pleistocene or Pliocene strata. The area immediately to the west appears to have subsided in Late Pleistocene (Chronis et al., 1991, Zelilidis, 2003). In the Rio Strait, there is little or no sediment accumulation because of powerful tidal flows, which transport sediment to both the Corinth and Patras basins.

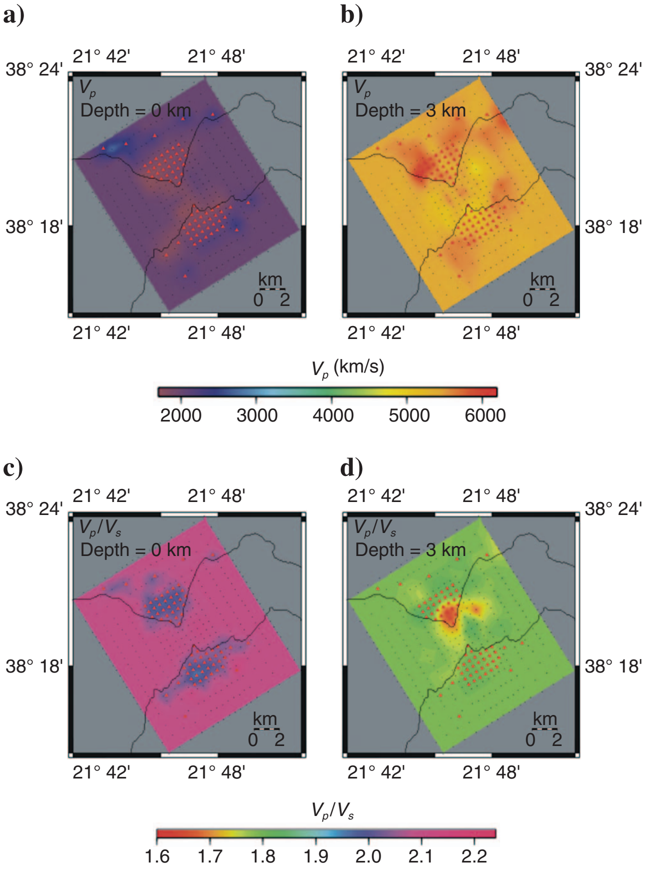

Figure 12. Plan views of V_p (top) at (a) 0 and (b) 3 km depth and V_p/V_s models (bottom) at (c) 0 and (d) 3 km depth.

Checkerboard test

Synthetic checkerboards were generated by superposing a ±10% velocity perturbation on the 1D initial starting velocity models (Figure 13); it was applied in $1\times1\times1$ km model cells (1 km horizontally and 1 km vertically). Each transition from high to low velocity occurs over two model blocks because the regularization used in the inversion impedes the reconstruction of sharp velocity contrasts between model blocks.

Although the optimal horizontal wavelength in the checkerboard test is 1 km, structures with much shorter wavelength can be resolved by the data; e.g., the corners of the checkerboards are well imaged in the best-resolved regions. Synthetic traveltimes were calculated for the "real" experimental geometry, and we used the aforementioned synthetic velocity model with an added Gaussian noise of zero mean and a standard deviation of 0.05 s. In the reconstructions, the original 1D velocity models were used as starting models with the earthquake origin times and hypocentral locations randomly redistributed with zero mean Gaussian noise and with a 0.1 s and 1 km standard deviation, respectively.

Figures 14 and 15 contain the hit count, DWS, and RDE for the V_p and V_p/V_s models, respectively. On the basis of these tests, areas with hit count, DWS, and RDE values greater than 200, 1500, and 0.2, respectively, are considered as the best-resolved.

At the area of interest where the seismic network is very dense, the ray coverage and the recovery of synthetic velocity anomalies are very good near the surface as well as at 3 km depth (especially for the V_p model because of the significantly larger number of P-wave arrivals). Although the resolving power of data was reduced in the offshore part of the model related to the "network gap" as a result of budget limits, the successful recovery of the velocity anomaly indicates that, by adopting a graded inversion scheme, we were able to provide a reliable velocity model. At the periphery of the target area, some of the velocity anomalies are recovered but contain some smearing because of the sparseness of the seismic network.

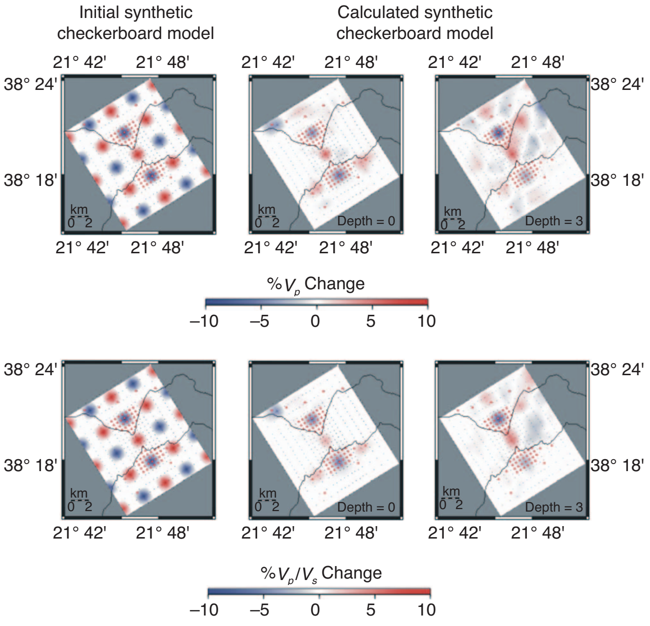

Figure 13. Checkerboard test for V_p (top) and V_p/V_s models (bottom). The velocity anomalies within the target area are well recovered.

CLUSTER ANALYSIS CLASSIFICATION

The combined results of seismic velocities from passive seismic tomography may provide a plausible basis for a lithological interpretation of the geophysical results. This can be achieved using a classification approach for the P-velocities and the Poisson's ratio (σ). The data used from the seismic tomography processing were the P-wave velocity and Poisson's-ratio models that were independently deduced. Only the sufficiently well-resolved parts of the results were selected and used for the representative cross sections (Figures 9 and 10). The data were analyzed using two different approaches.

Cluster analysis was first used to identify classes and to inspect the parameter 2D space (Bauer et al., 2003). The parameter space was divided into bins with constant spatial increments along each parameter axis ($\boldsymbol{\Delta\sigma_j}$, $\mathbf{\Delta V_{pj}}$) and characterized by their midpoints (σ_j and V_{pj}). In the next step, we calculated the relative frequency of the data samples falling into each bin using

$$f_r(\sigma_j, V_{pj}) = \frac{100}{n}\sum_{i=1}^{n} c_i, \tag{7}$$

where n is the total number of data pairs in the parameter space; $c_i = 1$ if i sample is in j bin, and $c_i = 0$ if i sample is not in j bin.

The calculated relative frequency for the sections presented in Figures 9 and 10 and for each one of the sections (profiles A1-A2, B1-B2, and C1-C2) shown in Figure 2 are depicted in Figures 16a-c, respectively. The relative frequency for the 3D volume of Figure 11a is presented in Figure 16d; there is a cluster close to the Poisson's ratio value of 0.2 and a P-wave velocity value of 5–5.51 km/s. The majority of points fall in the bins proximal to that point. Also, some less-prominent clusters are apparent in the diagram. A disadvantage of this method is that in this data set the clusters of the data are not clearly separated and their limits are difficult to define. The cluster classification results (Figure 16) reveal the existence of some major lithological units.

To further analyze the clustering of the data and to reveal the major lithological units in the region, we use Kohonen self-organizing maps (SOMs). These are unsupervised artificial neural networks developed by Kohonen (1995), who intended to provide ordered feature maps of input data after clustering (Chang et al., 2002; Ripley, 1996; Vesanto et al., 1999). That is, SOMs are capable of mapping high-dimensional, similar input data into clusters close to each other on an n-dimensional grid of neurons (units).

That grid forms what is known as the output space, whereas the input space is the original space where the data patterns exist. This mapping tries to preserve topological relations, that is, patterns that are close in the input space will be mapped to neurons that are close in the output space and vice versa. To provide even distances between units in the output space, hexagonal grids are often used (Bacao et al., 2005).

One of the basic distinctions between "classical" neural networks and SOMs is their ability to perform unsupervised learning. SOMs require no a priori information to function, and they excel at establishing unseen relationships in datasets (Penn, 2005). Once an SOM is trained for a specified data set, it can be applied to other similar data sets. The SOM-created vectors (codevectors) can then be used in a fashion similar to that of codebooks used in vector quantization to classify subsequent imagery data. Another salient feature of SOMs is their ability to preserve topology of a data set (Villmann et al., 1997).

Each input layer unit has as many weights or coefficients as the input patterns and, thus, can be regarded as a vector in the same space as the patterns. To train an SOM with a given input pattern, we calculate the distance between that pattern and every unit in the network, select the unit that is closest to the "winning unit," and accept that the pattern is mapped onto that unit. If the SOM has been trained successfully, then patterns that are close in the input space will be mapped to neurons that are close in the output space, and vice versa. Thus, SOM is "topology preserving" in the sense that neighborhoods are preserved through the mapping process (Bacao et al., 2005). The overall learning process of an SOM is accomplished through the iterative process depicted in Figure 17.

Fitting of model vectors is performed by sequential regression. The best match for each sample is subject to the condition

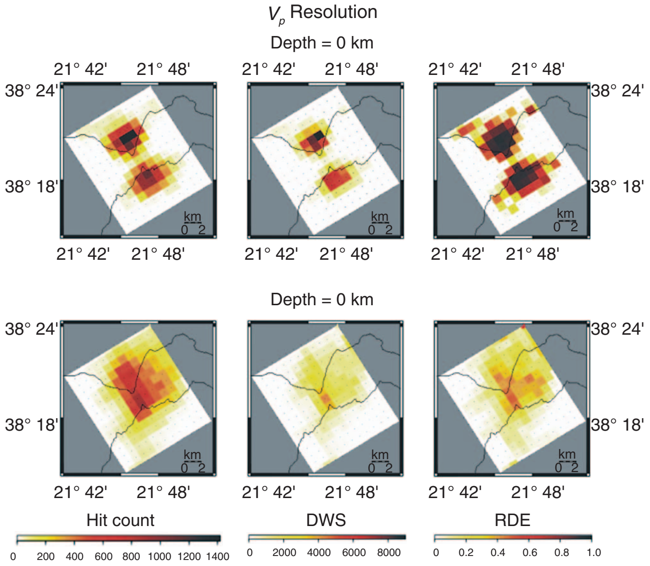

Figure 14. Resolution parameters at 0 km (top) and 3 km depth (bottom) for the P-wave velocity model.

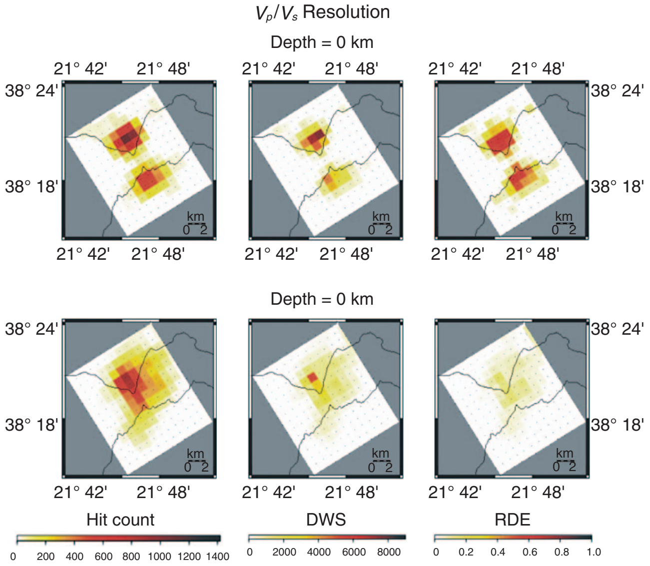

Figure 15. Resolution parameters at 0 km (top) and 3 km depth (bottom) for the V_p/V_s model.

$$\forall i, \|x(t) - m_c(t)\| \leq \|x(t) - m_i(t)\|, \tag{8}$$

where t is the step index for each sample x. Then, all model vectors (or a subset of them) that belong to nodes around node $c = c(x)$ are updated by the relation

$$m_i(t+1) = m_i(t) + h_{c(x),i}[(x(t) - m_i(t))]. \tag{9}$$

In this formula, $h_{c(x),i}$ is the "neighborhood function," which decreases with increasing separation between the ith and cth nodes on the map grid. This regression is reiterated over the available samples (Kohonen, 1995) to find the optimal index c.

The initial step is to read all the component parameters of the data and to construct the component planes for each one of them (Figure 18a and c) as well as to calculate the unified distance matrix "U-matrix" (Figure 18a) using the SOM's codevectors as the data source (Davies and Bouldin, 1979). The U-matrix is a representation of an SOM in which distances in the input space between neighboring neurons are represented usually using a color scale. If distances between neighboring neurons are small, then these neurons represent a cluster of patterns with similar characteristics. If the neurons are far apart, then they are located in a zone of the input space that has few patterns and can be seen as a separation between clusters. The U-matrix constitutes a particularly useful tool to analyze the results of an SOM, as it allows an appropriate interpretation of the clusters available in the data.

There is a correlation of the high Poisson's ratios with low P-wave velocities that is consistent with the presence of sediments; towards the upper left corner (Figure 18), we can observe a correlation of low Poisson's ratio with high velocities, even though they are not the highest velocities that can be observed in the section.

The next step is to define and separate the clusters that are formed by the data (Figure 18d). For this, k-means are used to define the clustering of the data; from the average maximal distance of each cluster to the others, the Davies-Bouldin index (Davies and Bouldin, 1979) is calculated. This index is used as a measure of the cluster separation.

Next, the results from the classification process are mapped to the depth sections (profiles C1-C2, B1-B2, and A1-A2) in Figure 3 and are presented in Figure 19. The separation of the major lithological units is obvious.

The low-P-wave-velocity cluster (cluster 1 in Figure 19) corresponds to the soft, lower Pleistocene sediments in Figures 8a and 10a. Clusters 2 and 3 correspond to flysch formations; cluster 4 traverses the main bedrock volume and is characterized by high P-wave velocity and low Poisson's ratio. There are indications, as described below, that Cluster 5 may be related to an evaporite body.

Figure 9a, which presents the P-wave velocity cross section across the Rio-Antirio axis, shows a high-velocity feature. This feature is more obvious in the Poisson's ratio data (Figure 9b); it appears as a low-Poisson's-ratio anomaly. Areas characterized by P-wave velocities from 4.8 to 5.3 km/s and a V_p/V_s ratio from 1.6 to 1.70 correspond to evaporites (Tatham, 1982; Domenico, 1984) and suggest the existence of an evaporite body in the area. The same conclusion can be reached from Figure 10.

To further investigate the 3D distribution of the derived clusters over the entire region, we performed SOM analysis in the 3D V_p, V_s, and Poisson's-ratio space. Because only two of these parameters are

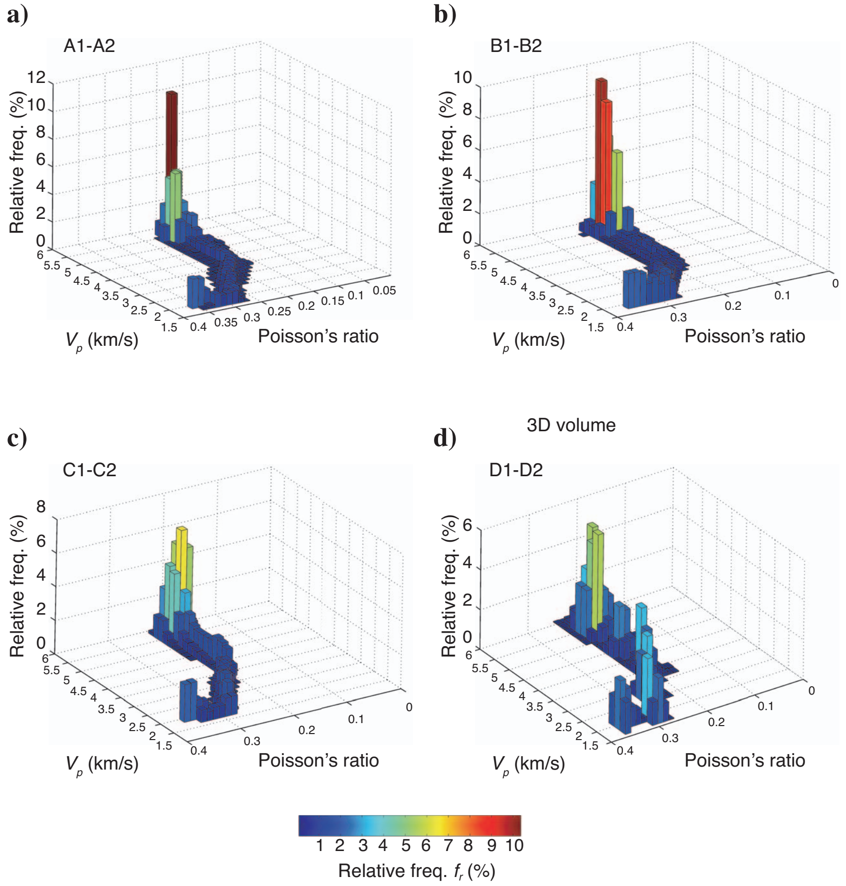

Figure 16. The V_p-Poisson's ratio parameter space divided in bins; the relative 3D histogram shows the relative frequency for each bin along profiles A1-A2, B1-B2, C1-C2 and for the entire 3D volume.

required to get the third one, one might think that training the SOM with two of them is adequate. Klose (2003) proved that the results are further improved if we use all the above parameters. A visualization of the procedure followed is presented in Figure 20.

The corresponding 3D mapping of the data clusters is presented in Figure 21a and c. Figure 21 shows cluster 5, which was not previously seen in the velocity tomographic results. Drilling data in the Gulf of Patras penetrated evaporites at a depth of 1850 m (Sotiropoulos et al., 2003). This is consistent with the results of the present investigation and with the results of magnetotelluric (MT) investigations (to be presented elsewhere); so, we interpret this anomaly as an evaporite body.

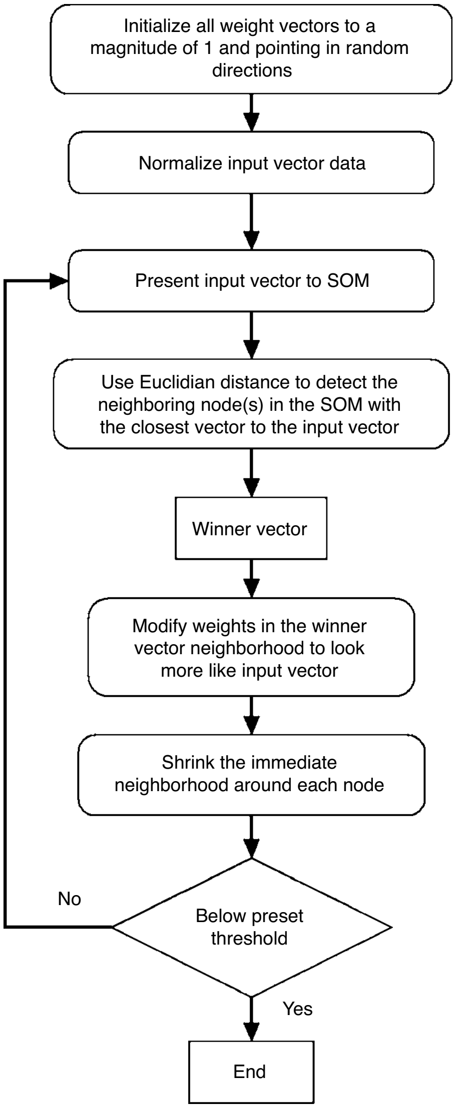

Figure 17. The training process of the SOM network.

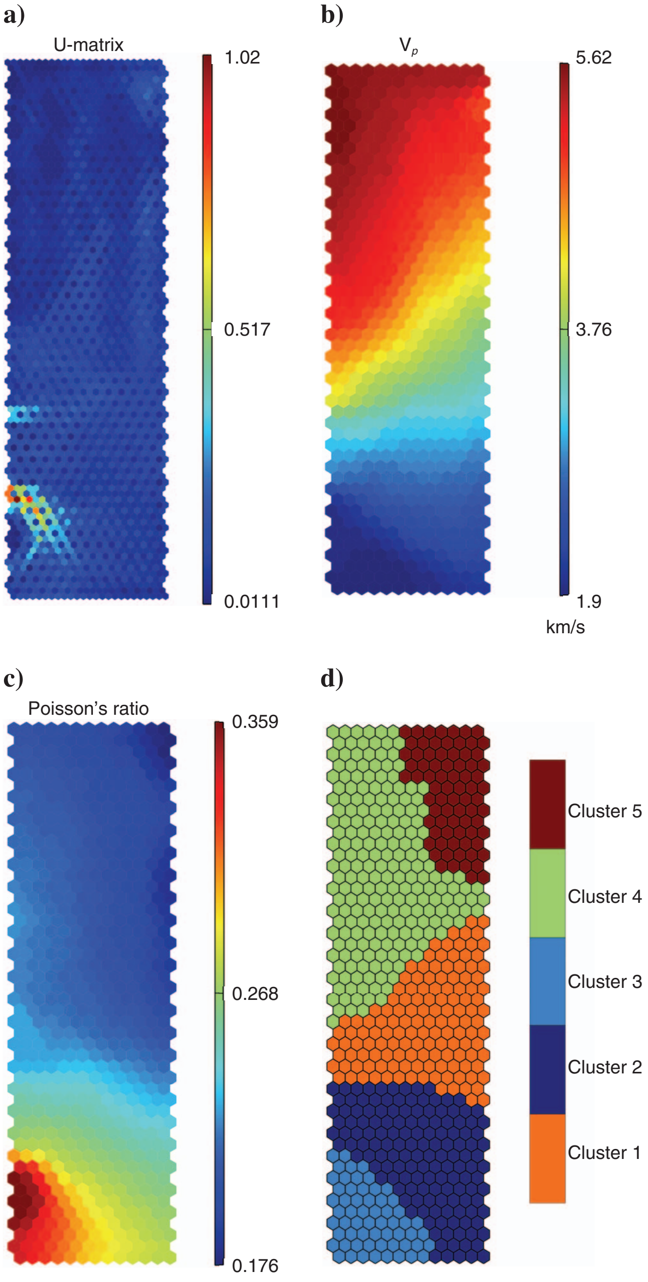

Figure 18. The component planes for (a) the U-matrix, (b) P-wave velocity, (c) Poisson's ratio, and (d) the clustering of the data.

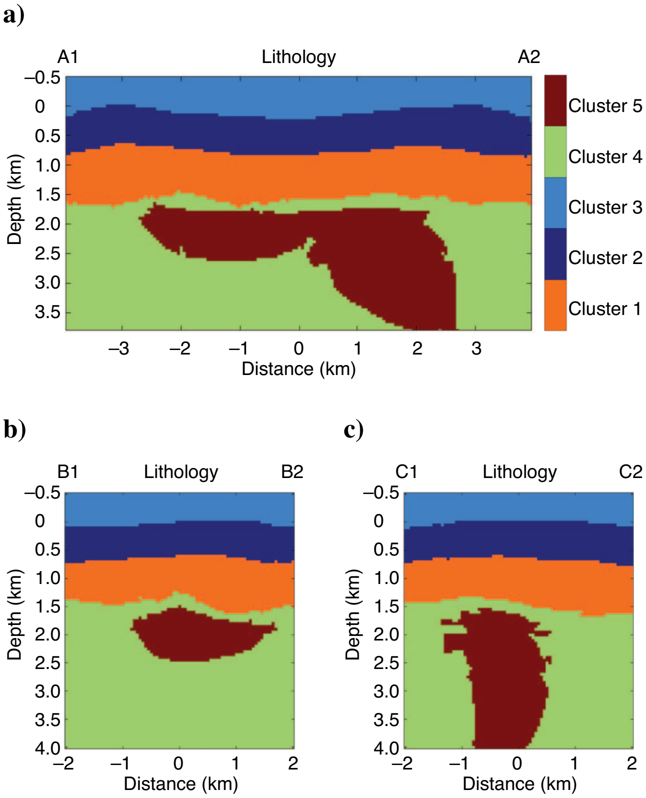

Figure 19. Mapping the data clusters on the depth section along profiles A1-A2, B1-B2, and C1-C2. Cluster 1 corresponds to soft sediments, clusters 2, 3, and 4 correspond to flysh and bedrock layers with varying properties, and cluster 5 corresponds to the assumed evaporite body, respectively.

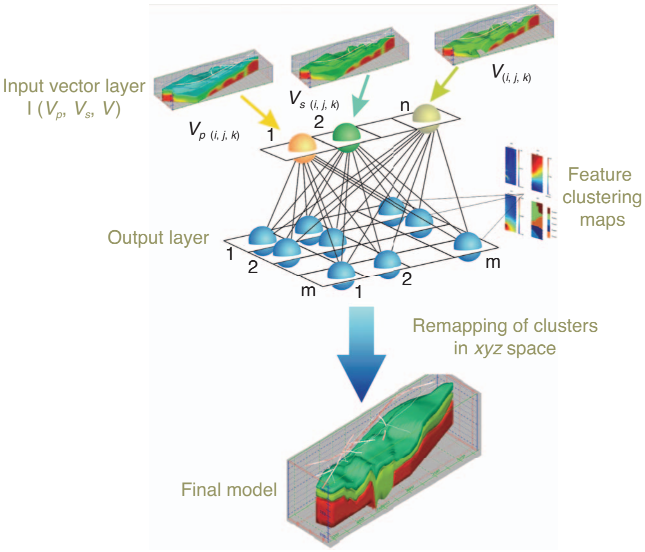

Figure 20. All three parameters — V_p, V_s, and Poisson's ratio — are used to train the SOM network in the present investigation and to obtain the lithological and structural model.

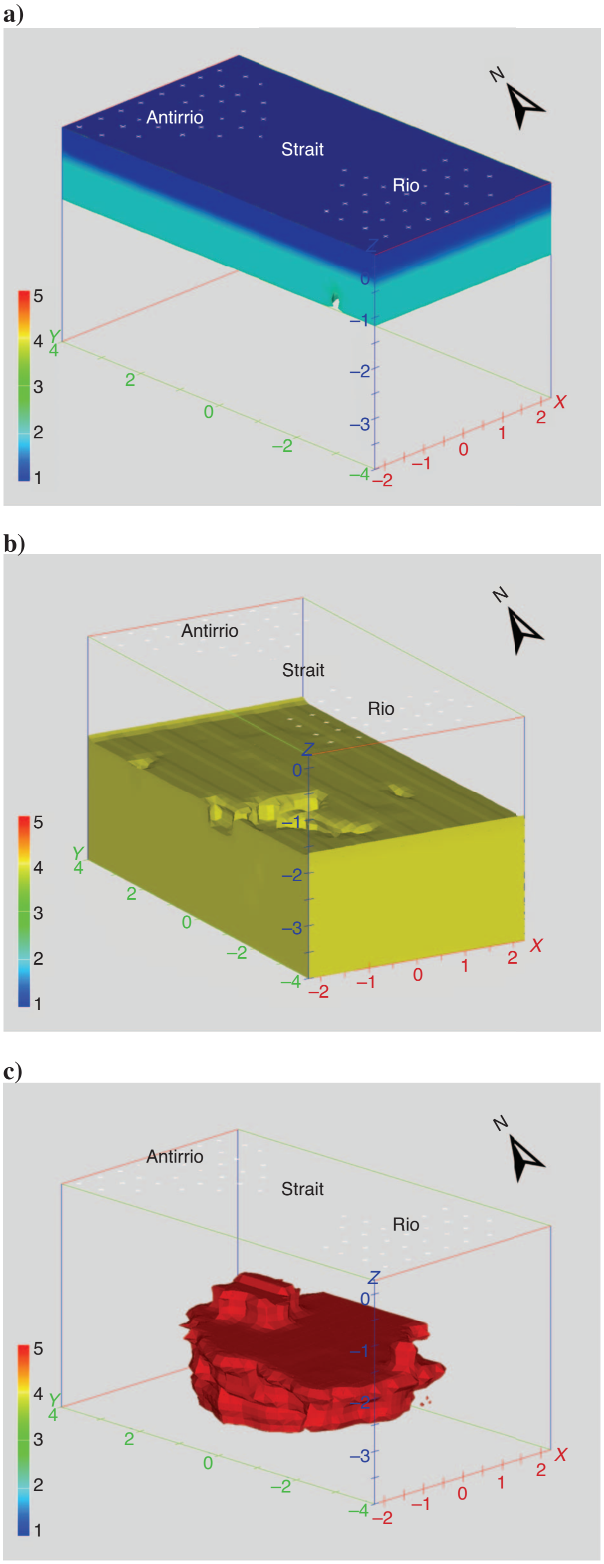

Figure 21. 3D-mapping of data clusters over the entire investigated area. (a) Clusters 1 and 2, (b) cluster 4 and (c) cluster 5, which is interpreted as an evaporite body.

CONCLUSIONS

Listening to the earth passively over time and using the collected information can provide structural and lithologic information of the subsurface. Data processing of passive seismic tomography data is more complicated than simply applying off-the-shelf 3D inversion algorithms. To get the best resolution of the geological formations at the lowest cost, we tap an arsenal of technology: from initial velocity-model selection to simultaneous earthquake hypocenter and 3D velocity-model inversion, and synthetic and real-data checkerboard tests.

We have described efficient acquisition and processing methodologies for high-resolution, passive seismic tomography surveying in the Rio Antirio Strait region. The observed velocity models were further processed by employing cluster and self-organization methodologies (SOMs), and the distribution of five lithological units was assessed. Results were in agreement with existing geological information.

The results show that the SOM approach can provide insight into complex relationships in passive seismic tomography data sets while preserving the internal topological relations and simultaneously producing a statistical model for the data set to facilitate its structural (V_p) and lithological (V_p/V_s) interpretation. The latter is very difficult to extract at such large scale from conventional seismic data.

Furthermore, the survey results revealed the existence of an evaporite body. The example shows that passive seismic tomography can be a valuable tool for hydrocarbon exploration, especially in the case of large areas or areas characterized by difficult geological regimes (thrust belts, seismic-penetration-problem areas, difficult topography, etc.).

By avoiding source effects and having cableless, single phones in a grid spacing of hundred(s) of meters, the environmental footprint is minimal. In hydrocarbon exploration in active seismic areas, especially on land, this method is attractive for unraveling the subsurface 3D structures and the lithologic bodies at a fraction of the cost of a conventional 3D seismic survey. In addition, the method can also be used to provide a 3D subsurface model to support the reprocessing of 2D and 3D seismic surveys.

ACKNOWLEGMENTS

We thank Sergio Chavez-Perez for his extensive review and his valuable comments on our paper. We also thank Albert van der Kallen, Kees Wapenaar, and two anonymous reviewers for their valuable comments. LandTech Enterprises and the Railway Organization of Greece (ROG) are acknowledged for permission to publish the results of this investigation. This research was supported in part by ROG and EC Grant STREP-2005-04043-3HAZ.

REFERENCES

Bacao, F., V. Lobo, and M. Painho, 2005, The self organizing map, the GeoSOM, and relevant variants for geosciences: Computers and Geosciences, **31**, 155–163.

Bauer, K., A. Schulze, T. Ryberg, S. V. Sobolev, and M. Weber, 2003, Classification of lithology from seismic tomography. A case study from the Messum igneous complex, Namibia: Journal of Geophysical Research, **108** B3, 2152.

Benz, H. M., B. A. Chouet, P. B. Dawson, J. C. Lahr, R. A. Page, and J. A. Hole, 1996, Three dimensional P and S wave velocity structure of Redoubt Volcano, Alaska: Journal of Geophysical Research, **101**, 8111–8128.

Bernard, P., 1997, A low angle normal fault earthquake: The Ms = 6.2, June 1995 Aigion earthquake (Greece): Journal of Seismology, **1**, 131–150.

Brooks, M., J. E. Clews, N. S. Melis, and J. R. Underhill, 1988, Structural development of Neogene basins in western Greece: Basin Research, **1**, 129–138.

Chang, H-C., D. Kopaska-Merkel, and H-C. Chen, 2002, Identification of lithofacies using Kohonen self-organizing maps: Computers and Geosciences, **28**, 223–229.

Chiarabba, C., and A. Amato, 2003, Vp and Vp/Vs images in the Mw 6.0 Colfiorito fault region (central Italy): A contribution to the understanding of seismotectonic and seismogenic processes: Journal of Geophysical Research, **108**, 2248–2264.

Chronis, G., D. Piper, and G. Anagnostou, 1991, Late Quaternary evolution of the Gulf of Patras, Greece: Tectonism, deltaic sedimentation and sea level change: Marine Geology, **97**, 191–199.

Davies, D. L., and W. Bouldin, 1979, A cluster separation measure: IEEE Transactions on Pattern Analysis and Machine Intelligence, **1**, 224–227.

Domenico, S. N., 1984, Rock lithology and porosity determination from shear and compressional wave velocity: Geophysics, **49**, 1188–1195.

Doutsos, T., N. Kontopoulos, and G. Ferentinos, 1985, Das westlische Ende des Korinth-Grabens: Jahrbuch für Geologie und Pälaontologie, Monatshefte, **11**, 652–666.

Doutsos, T., N. Kontopoulos, and G. Poulimenos, 1988, The Corinth-Patras rift as the initial stage of continental fragmentation behind an active island arc (Greece): Basin Research, **1**, 177–190.

Doutsos, T., and G. Poulimenos, 1992, Geometry and kinematics of active faults and their seismotectonic significance in the western Corinth-Patras rift (Greece): Journal of Structural Geology, **14**, 689–699.

Durham, L. S., 2003, Passive seismic. Listen: Is it the next big thing?: AAPG, Explorer, 127–131.

Eberhart-Phillips, D., 1986, Three dimensional velocity structure in northern California coast ranges from inversion of local earthquake arrival times: Bulletin of the Seismological Society of America, **76**, 1025–1052.

———, 1990, Three-dimensional P and S velocity structure in the Coalinga region, California: Journal of Geophysical Research, **95**, 15342–15363.

Eberhart-Phillips, D., and A. J. Michael, 1998, Seismotectonics of the Loma Prieta, California, region determined from three-dimensional Vp, Vp/Vs, and seismicity: Journal of Geophysical Research, **103**, 21009–21120.

Eberhart-Phillips, D., and M. Reyners, 1997, Continental subduction and three dimensional crustal structure: The northern South Island, New Zealand: Journal of Geophysical Research, **102**, 11843–11861.

Ferentinos, G., M. Brooks, and T. Doutsos, 1985, Quaternary tectonics in the Gulf of Patras, Western Greece: Journal of Structural Geology, **7**, 713–717.

Flotté, N., S. Denis, M. Carla, and T. Julien, 2005, Along strike changes in the structural evolution over a brittle detachment fault: Example of the Pleistocene Coringh-Patras rift (Greece): Tectonophysics, **403**, 77–94.

Gomberg, J. S., K. M. Shedlock, and S. W. Roecker, 1990, The effect of S-wave arrival times on the accuracy of hypocenter estimation: Bulletin of the Seismological Society of America, **80**, 1605–1628.

Haslinger, F., E. Kissling, J. Ansorge, D. Hatzfeld, E. Papadimitriou, V. Karakostas, K. Makropoulos, H.-G. Kahle, and Y. Peter, 1999, 3D crustal structure from local earthquake tomography around the Gulf of Arta (Ionian region, NW Greece): Tectonophysics, **304**, 201218.

Hatzfeld, D., D. Kementzetzidou, V. Karakostas, M. Ziazia, S. Nothard, D. Diagourtas, A. Deschamps, G. Karakaisis, P. Papadimitriou, M. Scordilis, R. Smith, N. Voulgaris, S. Kiratzi, K. Makropoulos, M. P. Bouin, and P. Bernard, 1996, The Galaxidi earthquake of 18 November 1992: A possible asperity within the normal fault system of the gulf of Corinth (Greece): Bulletin of the Seismological Society of America, **86**, 1987–1991.

Humphreys, E., and R. W. Clayton, 1988, Adaptation of back projection tomography to seismic travel time problems: Journal of Geophysical Research, **93**, 1073–1085.

Iyer, H. M., and K. Hirahara, 1993, Seismic tomography: Theory and practice: Chapman and Hall.

Kapotas, S., G-A. Tselentis, and N. Martakis, 2003, Case study in NW Greece of passive seismic tomography: A new tool for hydrocarbon exploration: First Break, **21**, 37–42.

Kissling, E., 1988, Geotomography with local earthquake data: Reviews of Geophysics, **26**, 659–698.

Kissling, E., W. L. Ellsworth, D. Eberhart-Phillips, and U. Kradolfer, 1994, Initial reference models in local earthquake tomography: Journal of Geophysical Research, **99**, 19635–19646.

Kissling, E., S. Solarino, and M. Cattaneo, 1995, Improved seismic velocity reference model from local earthquake data in northwestern Italy: Terra Nova, **7**, 528–534.

Klose, C. D., 2003, Engineering geological rock mass characterization of granitic gneisses based on seismic in-situ measurements: Ph.D. thesis, Swiss Federal Institute of Technology.

Kohonen, T., 1995, Self-organizing maps: Springer.

Kontopoulos, N., and T. Doutsos, 1985, Sedimentology and tectonics of the Antirion area (Western Greece): Bollettino della Società Geologica Italiana, **104**, 479–489.

Kradolfer, U., 1989, Seismische tomographie in der Schweiz mittels lokaler erdbeben: Ph.D. thesis, ETH.

Lahr, J. C., 1989, Hypoellipse/Version 2.0: A computer program for determining local earthquake hypocentral parameters, magnitude, and first motion pattern: Open-File Report, 89-116, U. S. Geological Survey.

Lanczos, C., 1961, Linear differential operators: D. Van Norstand Co.

Latorre, D., J. Virieux, T. Monfret, V. Monteiller, T. Vanorio, J-L. Got, and H. Lyon-Caen, 2004, A new seismic tomography of Aigion area (Gulf of Corinth, Greece) from the 1991 data set: Geophysical Journal International, **159**, 1013–1031.

Lee, W. H., and S. W. Stewart, 1981, Principles and applications of microearthquake networks: Advances in geophysics, supplement 2: Academic Press.

Le Meur, H., J Virieux., and P. Podvin, 1997, Seismic tomography of the Gulf of Corinth: A comparison of methods: Annales de Geophysique, **XL**, 1–25.

Lyon-Caen, H., P. Papadimitriou, A. Deschamps, P. Bernard, K. Makropoulos, F. Pacchiani, and G. Patau, 2004, First results of CRLN seismic array in the western Corinth rift: Evidence for old fault reactivation: Comptes Rendus Geoscience, **336**, 343–351.

Martakis, N., S. Kapotas, and G-A. Tselentis, 2006, Integrated passive seismic acquisition and methodology: Case studies: Geophysical Prospecting, **54**, 1–19.

Melis, N. S., P. W. Burton, and M. Brooks, 1995, Coseismic crustal deformation from microseismicity in the Patras area, western Greece: Geophysical Journal International, **122**, 815–836.

Melis, N. S., and G-A. Tselentis, 1998, 3-D P-wave velocity structure in western Greece determined from tomography using earthquake data recorded at the University of Patras seismic network (PATNET): Pure and Applied Geophysics, **152**, 329–348.

Michelini, A., 1993, Testing the reliability of Vp/Vs anomalies in travel time tomography: Geophysical Journal International, **114**, 405–410.

Novotny, O., J. Zahradnik, and G-A. Tselentis, 2001, Northwestern Turkey earthquakes and the crustal structure inferred from surface waves observed in the Corinth Gulf, Greece: Bulletin of the Seismological Society of America, **91**, 875–879.

Penn, B. S., 2005, Using self-organizing maps to visualize high-dimensional data: Computers and Geosciences, **31**, 531–544.

Rigo, A., H. Lyon-Caen, R. Armijo, A. Deschamps, D. Hatzfeld, K. Makropoulos, P. Papadimitriou, and I. Kassaras, 1996, A microseismic study in the western part of the Gulf of Corinth (Greece): Implications for large-scale normal faulting mechanisms: Geophysical Journal International, **126**, 663–688.

Ripley, B. D., 1996, Pattern recognition and neural networks: Cambridge University Press.

Sorel, D., 2000, A Pliocene and still-active detachment fault and the origin of the Corinth-Patras rift, Greece: Geology, **28**, 83–86.

Sotiropoulos, S., E. Kamberis, M. Triantaphyllou, and T. Doutsos, 2003, Thrust sequences in the central part of the external Hellenides: Geological Magazine, **140**, 661–668.

Tatham, R. H., 1982, Vp/Vs and lithology: Geophysics, **47**, 336–344.

Thurber, C. H., 1983, Earthquake locations and three-dimensional crustal structure in the Coyote Lake area, central California: Journal of Geophysical Research, **88**, 8226–8236.

———, 1986, Analysis methods for kinematic data from local earthquakes: Reviews of Geophysics, **24**, 793–805.

———, 1993, Local earthquake tomography: Velocities and Vp/Vs theory, *in* H. M. Iyer and K. Hirahara, eds., Seismic tomography — Theory and practice: Chapman and Hall, 563–583.

Thurber, C. H., S. R. Atre, and D. Eberhart-Phillips, 1995, Three-dimensional Vp and Vp/Vs structure at Loma Prieta, California, from local earthquake tomography: Geophysical Research Letters, **22**, 3079–3082.

Toomey, D. R., and G. R. Foulger, 1989, Tomographic inversion of local earthquakes data from the Hengill-Grendsalur Central Volcano Complex, Iceland: Journal of Geophysical Research, **94**, 17497–17510.

Tryggvason, A., S. Rognvaldsson, and O. Flovenz, 2002, Three-dimensional imaging of the P- and S-wave velocity structure and earthquake location beneath southwest Iceland: Geophysics Journal International, **151**, 848–866.

Tselentis, G-A., and C. Makropoulos, 1986, Rates of crustal deformation in the Gulf of Corinth (central. Greece) as determined from seismicity: Tectonophysics, **124**, 55–66.

Tselentis, G-A., and G. Stavrakakis, 1987, A method of quantifying the dependence of the depth of the hypocenter of an earthquake upon the velocity model: Computers and Geosciences, **9**, 281–287.

Tselentis, G-A., I. Vasiliou, E. Lekkas, D. Roubos, and E. Sokos, 1998, Site specific design strong motions at the city of Vartholomio-Greece: 3rd Conference of Geotechnical Engineering, Proceedings, vol. I, 567–574.

Tselentis, G-A., and J. Zahradnik, 2000, The Athens earthquake of 7 September 1999: Bulletin of the Seismological Society of America, **90**, 1143–1160.

Um, J., and C. H. Thurber, 1987, A fast algorithm for two-point seismic ray tracing: Bulletin of the Seismological Society of America, **77**, 972–986.

Vesanto, J., E. Alhoniemi, J. Himberg, K. Kiviluoto, J. Parviainen, 1999, Self-organizing map for data mining in MATLAB: The SOM toolbox: Simulation News Europe, **25**, 54.

Villmann, T., R. Der, M. Herrmann, and T. M. Martinez, 1997, Topology preservation in self-organizing feature maps: Exact definition and measurement: IEEE Transactions on Neural Networks, **8**, 256–266.

Xanalatos, N., and G-A. Tselentis, 1997, SEISMWIN, an algorithm for processing seismological waveforms: Proceedings Geological Society Athens, **22**, 235–246.

Zelilidis, A., 2003, The geometry of fan-deltas and related turbidites in narrow linear basins: Geological Journal, **38**, 31–46.